RSC Advances

PAPER

View Article Online
View Journal | View Issue

Cite this: *RSC Adv.*, 2025, **15**, 28642

Light-mediated CO release from a tricarbonyl manganese(I) complex with a bidentate quinoxaline ligand

Rabaa M. Khaled, †[a] Krzysztof Radacki, [b] Gamal A. E. Mostafa,[c] Essam A. Ali,[c] Ola R. Shehab *[a] and Ahmed M. Mansour †*[ad]

Received 25th May 2025
Accepted 1st August 2025

DOI: 10.1039/d5ra03678j

rsc.li/rsc-advances

Reaction between 2-(pyridin-2-yl)quinoxaline (L) and [MnBr(CO)$_5$] afforded a dark-stable *fac*-[MnBr(CO)$_3$L] that releases CO upon exposure to visible light (468–525 nm). Different structural elucidation methods, including X-ray crystallography, were used to thoroughly characterize the structure of the organometallic compound. Prior to recording the profiles of dark-stability and photolysis in various organic solvents, the complex's solvatochromism features were examined experimentally and through quantum chemical calculations. As solutions become less polar, the lowest energy transition in DMSO, which is observed at 487 nm, is red-shifted, which could be explained by negative solvatochromism. Illuminating the pre-incubated solutions of the complex in organic solvents at 525 nm, with or without calf-thymus DNA, hen white egg lysozyme, or histidine, yields a two-step process perhaps associated with the sequential release of 3 CO molecules. In comparison, the principal factor influencing the CO release kinetics of the complex is the medium and the percentage of DMSO for example, with minimal interference from the biomolecules.

1. Introduction

The "silent killer" gas, carbon monoxide (CO), is recognized as a hazardous molecule owing to its significant affinity toward haemoglobin, which reduces the amount of oxygen that tissues can use.[1] To date, CO has been found to provide some biological advantages[2–5] at concentrations lower than 250 ppm.[6] Carbon monoxide has been proved to have vasodilating,[7] and heart-protective properties[8] in addition to its role as a neurological system signalling molecule. Conversely, vascular problems, diabetes, sepsis, and colitis have all been connected to CO shortage.[3,9] The development of prodrugs capable of delivering CO consistently and quantitatively may provide a novel technique to directly administer this medicinal gas, while addressing the disadvantage of unselective binding and distribution. Pharmaceutical chemists have had difficulty developing safe, workable approaches for giving therapeutic CO quantities, and this remains to be the case. Among the strategies utilised to deliver potentially effective amounts of CO to targeted tissues and organs, the development of organic and inorganic prodrugs named CO-releasing molecules (CORMs) is particularly intriguing. The frameworks, CO-releasing properties, and specific biological characteristics of the classes of CORMs were thoroughly investigated.[10–15] Metal carbonyl complexes (MCCs) are one of the intriguing families of metal-based CORMs; they have been thoroughly studied for their possible CO release characteristics and biological applications *e.g.*, antimicrobial,[15] and cytotoxic properties.[13] Different CO release mechanisms can be applied for MCCs such as ligand exchange in an aqueous media,[15] an alteration in pH,[16] a shift in redox state, enzymatically[17] or thermal heating.[18] When exposed to light, certain MCCs release CO. These molecules, known as "photoCORMs", the name launched by Ford,[19] provide a variety of benefits, which include the capacity to regulate the amount and timing of CO released. Based on the frequent worries over the usage of transition metal-based drugs, the metal employed in the synthesis of MCCs is significant. Due to their high degree of lability, MCCs of groups 3–5, and 10 have not been explored as CORMs. In contrast, the most appropriate metals for metal-based CORMs are those belonging to groups 6–9, with the exception of the radioactive element technetium.[13] In a recent review,[13] the frameworks, CO-releasing kinetics, and cytotoxic features of CORMs of 6–9 were thoroughly investigated. Manganese(I) based MCCs have drawn significant attention owing to their potential photo-chemical, and interesting biological uses. Actually, it is simple and highly controllable to replace the CO

[a]*Department of Chemistry, Faculty of Science, Cairo University, Gamma Street, Giza, 12613, Egypt. E-mail: Olashehab@sci.cu.edu.eg; Olashehab_chem@yahoo.com; mansour@sci.cu.edu.eg*

[b]*Institut für Anorganische Chemie, Julius-Maximilians-Universität Würzburg, Am Hubland, D-97074 Würzburg, Germany*

[c]*Department of Pharmaceutical Chemistry, College of Pharmacy, King Saud University, Riyadh 11451, Saudi Arabia*

[d]*Department of Chemistry, United Arab Emirates University, Al-Ain, United Arab Emirates. E-mail: Mansour_am@uaeu.ac.ae; inorganic_am@yahoo.com*

† Equal contribution.

molecules in the manganese carbonyl precursor with a variety of ligand systems. In addition, Mn is widely present as a cofactor in a number of enzymes, including glutamine synthetase,[20] and superoxide dismutase.[21] There is alarming evidence that Mn is detrimental to the brain, therefore using drugs that contain this element needs to be done with caution. The neurotoxic effect of Mn is brought on by metal buildup in the brain, which causes a progressive extrapyramidal sickness similar to Parkinson's disease.

Over the last two decades among the most significant obstacles in the development of metal-based CORMs has been to enhance the ability of photoCORMs to release CO when subjected to visible light and consequently shield cells from ultraviolet light, which was used with the first generation of CORMs.[13–15] Mn(I) photoCORMs may liberate CO when given visible light if a highly conjugated system is chosen appropriately.[14] However, moving the Mn(I) photoCORMs' MLCT into the red region may coincide with the complex's instability while incubated in the dark. In order to fulfil the requirements of photoCORMs, which include dark stability, appropriate tissue penetration depth, and the potential to emit CO when given visible light, it would be ideal if the CORMs could release CO when illuminated with green light in the 520–570 nm range. Even after reviewing the few prior accomplishments in this vast and fascinating field pertaining to the chemistry of Mn(I) CORMs, scientists continue to face a number of intriguing problems with the chemical and biological characteristics of CORMs: which is more important in controlling for example the cytotoxicity against the normal cell lines, the parent CORM or the CO depleted species? Finding a CORM with unique qualities, such as water solubility, long-term stability in the presence and absence of biomolecules, and the capacity to release CO when subjected to green light, is the first step in the solution of these questions. In this contribution, experimental investigations of the photophysical and photo-chemical characteristics of a novel tricarbonyl manganese(I) complex **2** (Scheme 1) containing 2-(pyridin-2-yl)quinoxaline (**1**) ligand were supplemented by quantum chemical computations. We have chosen **1** as an auxiliary ligand for **2** because it offers a range of biological effects.[23–26] The solvatochromic characteristics of **2** were investigated by obtaining electronic absorption spectra in several solvents with diverse features, including hydrogen-bond donors and acceptors. Experiments were conducted to assess the stability of **2** in the dark with and without biomolecules like hen white egg lysozyme and calf-thymus DNA. The incubated solutions were then subjected to a 525 nm light source in order to examine the possibility of CO release from **2** as well as the function of these biomolecules in regulating the mechanism and kinetics of CO release. The quantification of the amount of released CO was done using the myoglobin assay.

2. Results and discussion

2.1. Synthesis and structural characterization

Scheme 1 illustrates that reacting *o*-phenylene diamine with 2-acetylpyridine in methanol, acidified with drops of glacial acetic acid, yielded 2-(pyridin-2-yl)quinoxaline (**1**).[22] Unlike the previously published method,[27] the quinoxaline derivative was obtained without a catalyst being added to the reaction mixture. The crystal structure of **1**,[28] and its dicarbonyl Ru(II) complex[22] has already been published elsewhere. Next, the reaction between **1** and $[MnBr(CO)_5]$, in acetone, afforded **2** (Scheme 1). Complex **2** was structurally characterized with various spectroscopic and analytical techniques. The infrared spectrum of **2** (Fig. S1) has two prominent stretching bands at 2021, and 1916 cm^{-1}, attributed to the three CO molecules' symmetrical and anti-symmetrical stretching modes configured in a *facial* arrangement. The electrospray ionization mass spectrum (Fig. S2) of **2**, in the positive mode, exhibited two unique peaks at *m*/*z* 771.0, and 344.2 assignable to $\{2M–Br\}^+$, and $\{M–Br\}^+$ (M: molecular formula), respectively. The ^1H NMR spectrum of **2** (Fig. S3), in $CDCl_3$, consists of 9 signals matching the molecular structure of **2**. Moreover, appropriate single crystals were acquired for X-ray crystallographic examination through the slow evaporation of **2** in an acetone solution. The crystallographic parameters are provided in Table S1. Fig. 1 displays a depiction of the molecular structure of **2** along with some of its chosen crystal data (bond lengths and bond angles). Crystallization of the complex occurs in a monoclinic crystal structure of $P2_1/c$ space group with $a = 15.124(2)$ Å, $b = 14.3822(13)$ Å, $c = 7.1663(7)$ Å and $\beta = 102.285(9)°$. The unit cell is made up of four molecules (Fig. S4). As Fig. 1 shows, the structure of **2** provided a clear proof of octahedral geometry, the *N*,*N*-bidentate nature of **1** [Mn–N1_6 = 2.029(4) Å and Mn–N1_7 = 2.083(3) Å] and placement of the three CO ligands in a *facial* mode around the metal centre [Mn–C1_1 = 1.814(4) Å, Mn–C2_1 = 1.813(5) Å, Mn–C3_1 = 1.798(4) Å]. As with the previously reported dicarbonyl Ru(II) complex of **1**, the Mn bond with pyridine's nitrogen is 0.054 Å shorter than the one with quinoxaline's nitrogen.[22] The *trans*-Mn–C bonds to the pyridine ring or axial Br^- ligand are the same length, but they are 0.015 Å longer than the third one that is *trans* to the nitrogen of quinoxaline. Since the photo release of CO from a tricarbonyl Mn(I) family is known to occur in a sequential manner,[14] beginning

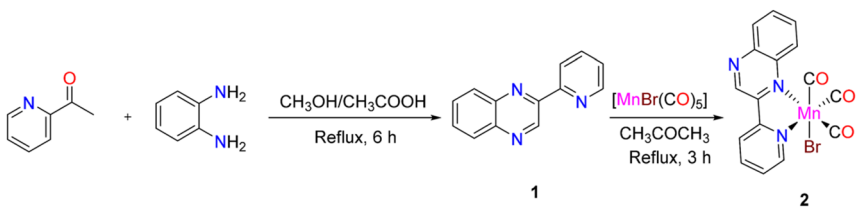

Scheme 1 Synthetic procedures of 2-(pyridin-2-yl)quinoxaline (**1**),[22] and its tricarbonyl Mn(I) complex (**2**).

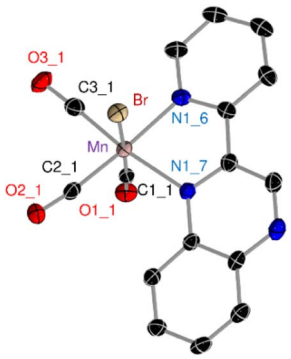

Fig. 1 Molecular structure of **2** (thermal ellipsoids are displayed at the 50% probability level). Bond lengths in Å: Mn–Br1_1 2.5275(8), Mn–N1_6 2.029(4), Mn–N1_7 2.082(3), Mn–C1_1 1.814(4), Mn–C2_1 1.813(5), Mn–C3_1 1.798(4), C1_1–O1_1 1.137(5), C2_1–O2_1 1.149(6), C3_1–O3_1 1.151(5). Bond angles (°): C1_1–Mn–Br1_1 178.1(2), C1_1–Mn–C2_1 92.3(2), C1_1–Mn–C3_1 88.1(2), C1_1–Mn–N1_6 96.4(2), C1_1–Mn–N1_7 92.7(2), Br1_1–Mn–C3_1 91.0(2), Br1_1–Mn–C2_1 86.0(1), Br1_1–Mn–N1_6 85.3(1), Br1_1–Mn–N1_7 88.3(1), C2_1–Mn–C3_1 85.2(2), C3_1–Mn–N1_6 94.6(2), C3_1–Mn–N1_7 173.4(2), C2_1–Mn–N1_6 171.3(2), C2_1–Mn–N1_7 101.3(2), N1_6–Mn–N1_7 78.9(1).

with the formation of photolabile dicarbonyl species, we anticipated that the weakly coordinated CO would be released first. In this instance, C1–O1 or C2–O2 may be the early loss from the coordination sphere, whereas C3–O3 should be the least. The analytical and spectroscopic tools indicated the synthesis of **2** in a pure form, with 3CO arranged in a *facial* mode and coordination of the quinoxaline ligand in a bidentate mode.

2.2. Hirshfeld surface analysis

Hirshfeld surface analysis[29] was executed on **2** to learn more about the intermolecular interactions through CrystalExplorer 17.5 software.[30] On the Hirshfeld surface, the white areas seen over *d*-norm (Fig. 2) signifies contacts separated by the sum of the van der Waals radii. Conversely, distances shorter than (near contact) or longer than (far contact) the total of the van der Waals radii are represented by red and blue, respectively. Fig. 2a displays the total two-dimensional fingerprint plots for **2**, while Fig. 2b–d display the O···H/H···O, N···H/H···N, and Br···H/H···Br contacts and their relative sharing to the Hirshfeld surface. As shown in Fig. 2b, the most noteworthy interactions in **2** are H···O/O···H (22.1%). The stabilisation of the crystal structure and molecular packing are significantly impacted by these interactions. The H···Br/Br···H interactions (Fig. 2d) emphasise the significance of hydrogen bonds including Br atoms in regulating the stability along with other physical qualities, as they comprise 12.4% of the surface. A 6.2% contribution to the stabilisation of the crystal structure is attributed to the H···N/N···H interactions. In **2**, the conventional hydrogen bond (A–H···B; A and B are electro-negative atoms) is absent, while the blue-shifting H-bond (C–H···B) is observed with the axial bromido ligand and the quinoxaline nitrogen play the main role as illustrated in Fig. S4.

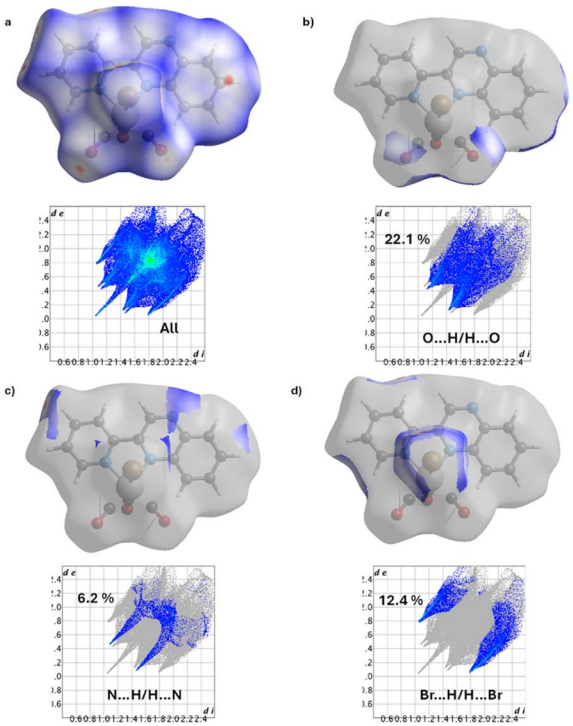

Fig. 2 The full two-dimensional fingerprint plots and their relative Hirshfeld surface for the most abundant interactions in **2**, demonstrating (a) all interactions, and delineated into (b) O···H/H···O, (c) N···H/H···N, (d) Br···H/H···Br interactions.

2.3. Electronic structure

The UV/Vis spectrum (Fig. 3) of **2**, in DMSO, is distinguished by a broad band at about 487 nm. This may be attributed to admixture of metal–ligand charge transfer (MLCT) towards CO ligands and LLCT (LLCT: ligand–ligand charge transfer).[31,32] To comprehend the characteristics of the band at 487 nm and solvatochromism properties, we recorded the electronic absorption spectra in other solvents with varied hydrogen bond tendency and polarity such as dichloromethane, acetonitrile, dimethylformamide tetrahydrofuran, methanol, and 1,4-dioxane. Complex **2** has a poor solubility in toluene. It is highly probable that the axial Br^- ion will exchange with coordinating

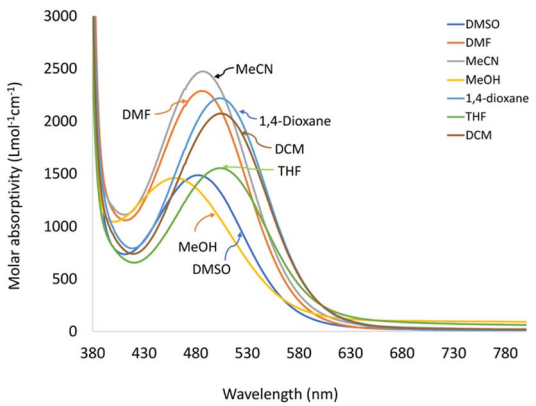

Fig. 3 UV/Vis spectra of **2** in various organic solvents.

solvents like DMSO and acetonitrile, and it might even be 1,4-dioxane.[33,34] This may affect where the lowest energy transition is positioned. The exchange process and the solvent effect appear to be at variance. As illustrated in Fig. 3, except for methanol, the lowest energy transition in DMSO, which is seen at 487 nm, is red-shifted in increasingly less polar solvents. There is a slightly change of about 2–5 nm on going from DMSO to DMF and then acetonitrile. Despite the high likelihood of axial ligand exchange, the location of the lowest energy band nevertheless noticeably shifts. This may be accounted for negative solvatochromism. For metal carbonyls, negative solvatochromism was explained by the reduced excited-state electric dipole.[35–37] The data show that the closely comparable reported Mn(I)-diamine complexes exhibit the same negative solvatochromism characteristic.[33,38]

To understand the nature of the observed electronic transitions, time-dependent density functional theory computations were done on the local minimum structure (Table S2) using two functionals, Becke 3-parameter Lee–Yang–Parr (B3LYP),[39,40] and a hybrid exchange-correlation functional named CAM-B3LYP.[41] LANL2DZ (Los Alamos National Laboratory 2-double-z) basis set and a universal solvation model (SMD),[42] were incorporated in the computation methods. With the help of TDDFT calculations, in the singlet state, we can understand the characteristics of the detected electronic absorption transitions. Table S3 lists the selected computed electronic transitions and their associated assignments. The electronic transitions (Table S3) estimated by B3LYP move to longer wavelengths than those found by CAM-B3LYP. The calculated spectrum of **2**, Fig. S5, at the B3LYP/LANL2DZ level of theory is distinguished by four bands at around 287, 335, 414, and 508 nm. As shown in Fig. 4, these absorption bands are developed corresponding to the following transitions: HOMO−4 → LUMO+1 (purple), HOMO−5 → LUMO (green), HOMO−4 → LUMO/HOMO−2 → LUMO (orange) and HOMO−1 → LUMO (red), respectively. The 508 nm transition, which differs slightly from the experimental transition, has a p(Br)/*d*(Mn) ground state and a mostly π(quinoxaline) excited state. As a result, the band at 508 nm can be allocated to MLCT/LLCT.[31,32] According to the explanations of the frontier molecular orbitals (FMOs) in Fig. 4, the bands at (287 and 414 nm) and 335 nm could be ascribed to MLCT/LLCT and LLCT, respectively. Alternatively, the CAM-B3LYP spectrum of **2** is featured by three bands at 256, 307, and 396 nm due to HOMO−2 → LUMO+1, HOMO−5 → LUMO and HOMO−1 → LUMO, respectively. By visualising the FMOs of the latter transitions (Table S4), the bands at 307 nm are attributed to LLCT, while the bands at 256 and 396 nm are allocated to MLCT/LLCT.

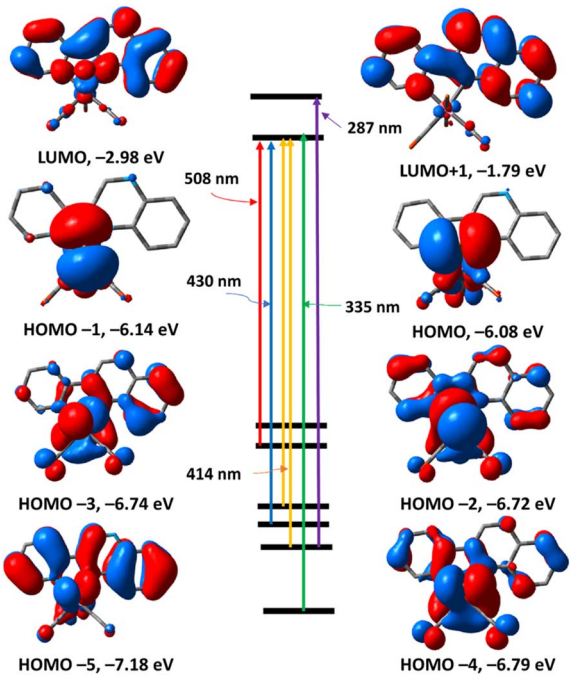

Fig. 4 Selected frontier molecular orbitals (FMOs) and calculated electronic transitions of **2**, which were calculated at B3LYP/LANL2DZ level of theory.

2.4. Carbon monoxide releasing features

2.4.1. In organic solvents. For possible medical uses, photoCORMs that liberate CO when exposed to light should have specific characteristics such as solubility in aqueous media, stability in the dark, the ability to release CO under illumination conditions as well as the biocompatibility.[42] When figuring out the rate of CO release and the type of CO-depleted fragments that are produced, the type of media is crucial. It is noteworthy that the rate of CO liberation was much slower in the water-based media, indicating that results from studies employing organic solvents might not readily apply to the biological or medical fields.[43,44] Additionally, to be biologically significant, photoCORMs and CO-depleted residues need to be safe, since the toxicity and nature of the generated metal fragments are dependent on the media in which they are created.[45] Initially, the stability of DMSO solution of **2** in the dark was investigated (Fig. S6). Complex **2** showed significant changes in its absorption spectrum over a 22 hour period when kept in the dark. The primary absorption band at 487 nm really loses half of its intensity. We can attribute the spectral change throughout the incubation to the exchange of Br^- ion with DMSO, as has been earlier noted with other Mn(I) complexes functionalised with some bidentate ligands,[33] since the 487 nm band was attributed to MLCT/LLCT (LLCT is mostly caused by Br^-). Next, the DMSO solution of **2** was then mixed with an excessive amount of NaBr to investigate the variation that was seen when the compound was incubated in the dark. The fluctuation in the intensity of the lowest energy transition at 487 nm upon the incubation in the dark is partially suppressed by the addition of sodium bromide (Fig. S7).

Illuminating the preincubated solution of **2** in DMSO at 525 nm results in a two-step process (Fig. 5). Initially, after 90 seconds of illumination, a clear isosbestic point at 535 nm appears (Fig. S8). The isosbestic point may reveal the presence of an equilibrium between *fac*-$Mn(CO)_3$ and *cis*-$Mn(CO)_2$ species. After that, there is a noticeable drop in the main transition's intensity for up to 18 min of illumination without any additional change (Fig. S8). According to some published research,[13,46] there is a stage where the axial ligand exchanges

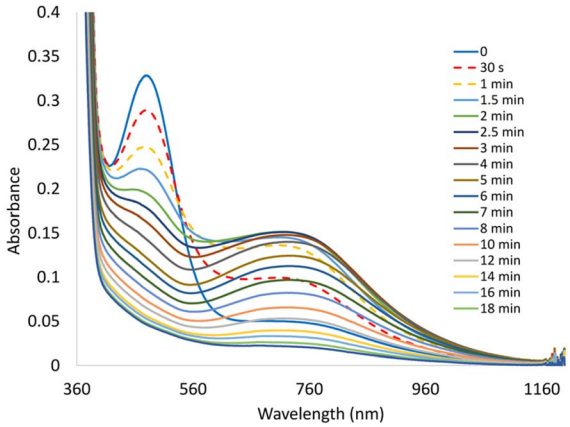

Fig. 5 UV/Vis spectral variations of the preincubated solution of **2** (0.30 mM in DMSO) by photolysis at 525 nm with illumination time of 18 min.

with the solvent molecule either prior to or following the initial CO molecule's release. This may have an impact on the CO release kinetics, as well as the type of the intermediates and CO-depleted species.

Similarly, we recorded the photolysis profile of treated DMSO solution of **2** (Fig. 6), with sodium bromide, under identical experimental conditions. Comparatively, the photolysis patterns of the DMSO solutions of **2** with and without NaBr do not change significantly. The first stage is achieved in 2.5 min with a clear isosbestic point at 526 nm (Fig. 6 and S9) and the plateau is attained in 40 min, suggesting that the kinetics are slower when NaBr is present. Since the addition of NaBr to the DMSO solution of **2** alters the wavelength of the developed isosbestic point, it appears that the nature of the intermediate in the two experiments listed above is different.

When water was added to the medium up to 30% of its polarity, the lowest energy transition in **2** moved slightly to 480 nm (Fig. S10). After 22 h in the dark, the solution of **2** exhibits a notable blue shift (~35 nm) in the main band position without any decrease in the band's intensity. This might result from **2** being completely hydrolysed and generation of the corresponding aqua tricarbonyl species. The liberation kinetics of CO from **2** in DMSO/H_2O mixture are considerably slower, reaching a plateau after 50 min (Fig. S11), although they nevertheless match those found in DMSO.

To look into how the solvent affects the CO releasing kinetics from **2**, acetonitrile was also used in the dark stability (Fig. S13 and S14) and photolysis experiment (Fig. 7). The position of the lowest energy point does not largely alter when DMSO is substituted with acetonitrile. It's interesting to note that after incubating the acetonitrile solution of **2** for 22 h, the intensity of the lowest energy band just slightly changes. The position of the lowest energy band remains unchanged, ruling out the possibility of axial ligand exchange with acetonitrile molecules.[43] The photo-chemical changes that are seen upon exposure to 525 nm follow two main stages, with a distinct isosbestic point at 534 nm, just like those that occur with DMSO and DMSO/H_2O media.

2.4.2. In the presence of biomolecules. In biological systems, carbon monoxide releasing molecules may interact with or bind to biomolecules before releasing CO. This could have an impact on the mechanism, kinetics, and characteristics of the CO depleted species that are produced. This interaction could alter their pharmacological activity and delivery.[47] While cisplatin and carboplatin primarily work by directly interacting with the double helix,[48] Lippard's group demonstrated that oxaliplatin destroys cells *via* causing ribosomal biogenesis stress.[49] The protein hen egg-white lysozyme, HEWL, has been shown in numerous studies to function as a biocompatible transporter for metal-based CORMs, transporting them intracellularly through its His15 side chain.[50–52] However, metal-based complexes that target DNA and have the capacity to bind and cleave it offer promising opportunities for the development of anticancer treatments. Therefore, understanding and evaluating the relationship between CORMs and DNA (or proteins) is essential for developing new chemotherapeutic medications.[53] For the reasons mentioned above, the dark stability of 70% DMSO/H_2O solutions of **2** in presence of histidine (Fig. S15), HEWL (Fig. S15), and calf thymus DNA (Fig. S15)

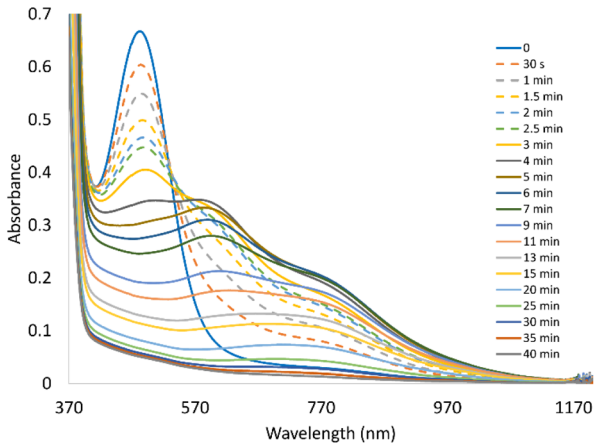

Fig. 6 UV/Vis spectral variations of the preincubated solution of **2**, treated with sodium bromide, (0.39 mM in DMSO) upon photolysis at 525 nm with illumination time of 40 min.

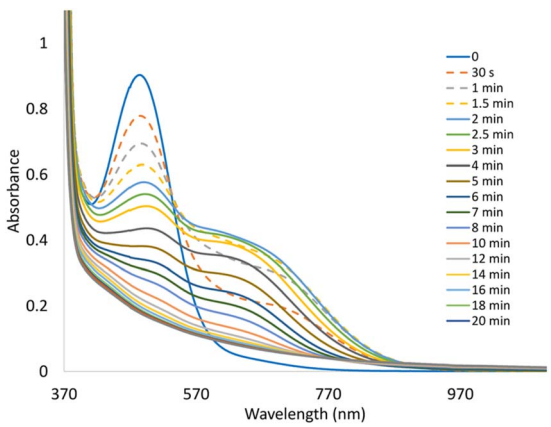

Fig. 7 UV/Vis spectral variations of the preincubated solution of **2** (0.51 mM in CH_3CN) upon photolysis at 525 nm with illumination time of 20 min.

were investigated. The profiles of dark stability of **2** in the presence and absence of HEWL and histidine are similar, excluding the possibility of any interaction between **2** and these biomolecules. In other words, the primary component affecting the dark stability profile of **2** is the media and the proportion of DMSO. When it comes to calf thymus DNA, the situation is entirely different. The lowest energy transition moves from 480 nm to 470 nm when DNA is added to a DMSO/H_2O solution of **2**, and it further blue shifts to 445 nm (Fig. S15). Comparatively, following 22 h of incubation of **2** with or without these biomolecules, the location of the lowest energy transition is almost identical (442–445 nm). It is noteworthy that the illumination profiles of **2** with and without these biomolecules are similar (Fig. 8, S16 and S17). As mentioned earlier, with regard to the photolysis done in the organic solvents, the CO release process of **2** involves two major steps, which could be related to stepwise CO release. The first stage is distinguished by the formation of an isosbestic point. According to the position of the developed isosbestic points, which are 505 nm for untreated, HEWL and DNA solutions, and 497 nm for histidine, we can presume that histidine might occupy the coordination sphere's empty position following the release of the first CO molecule.

2.4.3. In myoglobin solution. The myoglobin (Mb) test was utilised to quantify the amount of CO produced from **2** after being subjected to light with a wavelength of 525 nm.[54,55] Unfortunately, when the Mb solution of **2** was illuminated at 525 nm, the CO release kinetics were quite low (Fig. S18). About 6.5 μM MbCO was formed when the Mb solution of our photoCORM was exposed to 525 nm light with a rate constant of $(11.2 \pm 0.1) \times 10^{-4}$ s^{-1}, and $t_{1/2}$ of (10.31 + 0.02) min. As reported by us and other research groups, the rate of CO release was much slower in an aqueous solution, highlighting the possibility that findings from research utilising pure organic solvents could not be instantly appropriate to the biological or medical domains.[43,44] Additionally, recent studies have shown that the medium conditions can affect the type of iCORM and, thus, the CO release kinetics.[56] As a result, we chose to track the spectral variations in the Q-band after adding **2** and exposing it to a 468 nm light. About 10.0 μM MbCO was produced when the Mb solution of our photoCORM was exposed to 468 nm light with a rate constant of $(37.1 \pm 0.1) \times 10^{-4}$ s^{-1}, and $t_{1/2}$ of (4.39 + 0.10) min. Since only a small quantity of MbCO was produced throughout one hour of illumination, our Mn(I) photoCORM shows slow CO release kinetics.[46] This may add a benefit to **2**. CORMs with a short $t_{1/2}$ value may be unable to reach the body's desired target locations.[46]

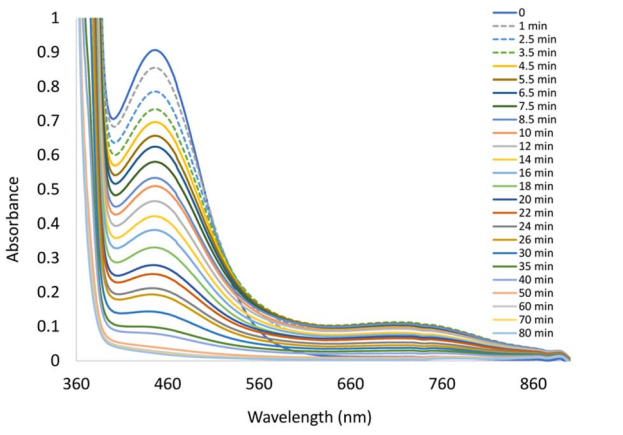

Fig. 8 UV/Vis spectral variations of the preincubated solution of **2** (0.39 mM in DMSO/H_2O in presence of CT-DNA) upon photolysis at 525 nm with illumination time of 80 min.

3. Conclusions

This work involved the synthesis and characterization of an interesting photoactivatable tricarbonyl manganese(I) complex functionalized with 2-(pyridin-2-yl)quinoxaline. Single-crystal X-ray diffraction analysis showed the unit cell of the complex is built of four molecules and the octahedron coordination sphere around Mn(I) is composed of 3 CO ligands arranged facially, one bromido ligand and a bidentate quinoxaline ligand. When the solvent polarity was altered from highly polar to less polar, negative solvatochromism behaviour was seen for the lowest energy band (*e.g.*, 487 nm in DMSO), which has an MLCT/LLCT character according to the quantum chemical calculations. The p(Br) orbital is the primary origin of the LLCT. The dark stability of the complex in different media (DMSO, 70% DMSO-H_2O and acetonitrile) in presence and absence of some biomolecules was examined. By incubating the DMSO solution of the complex overnight, we observed a significant reduction in the magnitude of the main absorption band that might be related to exchange of Br^- with DMSO. The rapid Br^--DMSO exchange has been partially suppressed by a common ion effect. This was not the case when acetonitrile was substituted for DMSO. Alternatively, when water was added to the DMSO solution up to 30% of its polarity, the lowest energy transition at 487 nm, seen in DMSO, moved slightly to 480 nm. After the dark incubation, the charge transfer band of the complex exhibits a notable blue shift (~35 nm) without any decrease in the band intensity. Similar behaviour was observed when HEWL or histidine was added to DMSO-water solutions, excluding the probability of any interaction between **2** and these biomolecules in presence of powerful coordinating solvent such as DMSO. It is noteworthy that the illumination profiles of the complex with and without these biomolecules are similar proceeding through two main stages due to the stepwise release of 3 CO molecules. In comparison, the medium and the proportion of DMSO, for instance, have the greatest influence on the complex's CO release kinetics, with biomolecules such as CT-DNA and HEWL having little effect.

4. Experimental

4.1. Materials and instruments

Sigma supplied all of the chemicals used in this study, including $[MnBr(CO)_5]$, which were used exactly as supplied. 2-(Pyridin-2-yl)quinoxaline was prepared following the published method.[22] The IR and NMR (^1H and ^{13}C) spectra were obtained from a Bruker Alpha-E instrument and a Bruker-Advance 400

MHz spectrometer, respectively. The electronic spectra of **2** in various solvents and under the effect of 525 nm light were obtained from a Specord 210 Plus spectrophotometer. In the positive mode, the ESI MS of the tricarbonyl Mn(I) complex was recorded with an Advion compact mass spectrometer. The micro elemental analysis of **2** was executed using a Vario EL III Elementar automatic CHNS analyzer.

4.2. Synthesis of [MnBr(CO)$_3$(2-(pyridin-2-yl)quinoxaline)]

To a round-bottomed flask loaded with [MnBr(CO)$_5$] (106 mg, 0.38 mmol) and 2-(pyridin-2-yl)quinoxaline (119 mg, 0.38 mmol), was added acetone (15 mL). In the absence of light, the reaction mixture was heated to reflux for 3 h. As the solvent slowly evaporated, a red precipitate formed. The precipitate was collected, washed with diethyl ether (3 × mL) and thereafter placed in a vacuum for four days. Yield: 87% (143 mg, 0.34 mmol). IR (ATR): ν = 2021 (*vs.*, C≡O), 1916 (*vs.*, C≡O), 1600, 1477, 1211, 1147, 777, 628 cm^{-1}. ^{1}H NMR (400.40 MHz, CDCl$_3$): δ = 9.59 (s, 1H, C=N–H, quinoxaline-H3), 9.47 (d, $^3J_{H,H}$ = 5.24 Hz, 1H, pyridine-H6), 9.06 (d, $^3J_{H,H}$ = 8.96 Hz, 1H, pyridine-H3), 8.48 (d, $^3J_{H,H}$ = 8.49 Hz, 1H, quinoxaline-H8), 8.30 (d, $^3J_{H,H}$ = 8.68 Hz, 1H, quinoxaline-H5), 8.16 (t, $^3J_{H,H}$ = 8.16 Hz, 1H, pyridine-H4), 8.06 (t, $^3J_{H,H}$ = 7.88 Hz, 1H, quinoxaline-H6), 8.02 (t, $^3J_{H,H}$ = 7.68 Hz, 1H, quinoxaline-H7) and 7.67 (t, $^3J_{H,H}$ = 5.86 Hz, 1H, pyridine-H5) ppm. ^{13}C NMR (100.10 MHz, CDCl$_3$/DMSO-d_6): δ = 154.3, 152.5, 151.0, 141.7, 141.4, 141.2, 137.8, 131.1, 130.7, 129.3, 126.4, 125.8, 124.3 ppm. ESI-MS (positive mode, acetone): m/z = 771.0 {2M–Br}$^+$, and 344.2 {M–Br}$^+$ (M: molecular formula). $C_{16}H_9BrMnN_3O_3$: C 45.10, H 2.13, N 9.86 found: C 44.93, H 2.01, N 9.59.

4.3. Single crystal X-ray diffraction analysis

During a two-week period, acetone solution of the metal complex slowly evaporated, resulting in orange plates appropriate for single crystal X-ray diffraction analysis. The diffraction results were obtained at 100 K by a RIGAKU XtaLAB Synergy-R diffractometer provided with a semiconductor HPA-detector (HyPix-6000) and multi-layer mirror mono-chromated Cu-Kα radiation. The intrinsic phasing approach (SHELXT programme) was exploited to solve the framework of the metal complex,[57] which was afterward enhanced by the SHELXL programme and the SHELXLE graphical user interface.[58] Non-hydrogen atoms were refined by an anisotropic approximation, while hydrogen atoms were 'riding' on idealised sites. Two-component twin refinement was applied to the data. Component 2 is rotated by 12° around [0.03–0.01–1.00] direct axis. The BASF parameter was refined to 5.6%. Crystal data for the complex: $C_{16}H_9BrMnN_3O_3$, M_r = 426.11, clear orange plate, 0.290 × 0.147 × 0.015 mm^3, monoclinic space group $P2_1/c$, a = 15.124(2) Å, b = 14.3822(13) Å, c = 7.1663(7) Å, β = 102.285(9)°, V = 1523.1(3) Å^3, Z = 4, ρ_{calcd} = 1.858 g·cm^{-3}, μ = 10.314 mm^{-1}, $F(000)$ = 840, T = 100(2) K, R_1 = 0.0542, wR_2 = 0.1593, 7082 independent reflections [$2\theta \leq 150.78°$] and 218 parameters. CCDC 2453856 includes supplementary crystallographic data for the present work.

4.4. Time dependent density functional calculations

The starting coordinates for the full optimisation process were taken from the complex's X-ray crystallographic data. In the ground state, vibrational analysis and geometry optimization of the tricarbonyl manganese(I) complex **2** were done by B3LYP functional,[39,40] and LANL2DZ basis set.[59,60] A similar methodology is commonly reported in the literature for DFT calculations of metal-based compounds.[61,62] It was verified that the complex's local minimum structure was found to be the lowest on the potential energy surface, according to the vibrational modes. Table S2 includes the atomic coordinates for the local minimum structure of **2**. The computed vibrational spectrum of **2** is shown Fig. S5. TDDFT computations were carried out using B3LYP/LANL2DZ/SMD and CAM-B3LYP[41]/LANL2DZ/SMD methods. All the calculations were executed by Gaussian03,[63] and the spectra (electronic and vibrational) as well as frontier molecular orbitals were visualized by Gaussview03.[64]

4.5. CO release investigation

Irradiation experiments in the organic solvents in presence and absence of biomolecules were carried out by a custom-built LED of 525 nm (λ_{peak} = 515 nm, $\Delta\lambda$ = 30 nm) light source (Kingbright Elec. Co., 6500 mcd, part. no. L-34ZGC). The photo-flow of the employed light sources was determined using ferrioxalate actinometry.[65] The quantum flow of the 525 nm source was about 6.69 × 10^{-11} Einstein per s. The capped cuvette was situated perpendicular to the LED at 3 cm. Using a Specord 210 Plus spectrophotometer, the electronic absorption spectra were obtained by turning off the illumination at regular intervals until no more changes were observed.

As previously described,[54,55] the myoglobin (Mb) assay was employed to spectrophotometrically assess the CO equivalents emitted by the tricarbonyl manganese(I) photoCORM by monitoring the mono carbonylation of Mb molecules. The stock solutions' concentrations were chosen to provide a final mixture of 10 μM sodium dithionite (reducing agent), 60 μM Mb, and 10 μM photoCORM. Both 525 and 468 nm (Kingbright Elec. Co., 5000 mcd, part. no. BL0106-15-299) were used in the myoglobin assay. The quantum flow for 468 nm LED source was found to be about 1.25 × 10^{-9} Einstein per s.

Author contributions

R. Khaled: methodology, investigation, validation. K. Radacki: methodology, investigation, resources. O. Shehab: investigation, writing – review & editing. G. Mostafa, writing – review & editing, resources. E. Ali, writing – review & editing, resources. A. Mansour: conceptualization, investigation, validation, resources, formal analysis, software, writing – original draft, writing – review & editing.

Conflicts of interest

The authors declare that they have no known competing financial interests or personal relationships that could have appeared to influence the work reported in this paper.

Data availability

The data supporting this article have been included as part of the SI.

CCDC 2453856 contains the supplementary crystallographic data for this paper.[66]

Supplementary information includes spectroscopic and quantum chemical calculations data. See DOI: https://doi.org/10.1039/d5ra03678j.

Acknowledgements

The authors would like to extend their sincere appreciation to the Ongoing Research Funding program (ORF-2025-1000), King Saud University, Riyadh, Saudi Arabia, for financial support. The authors would like to thank United Arab Emirates University, Al Ain, UAE, for research support.

Notes and references

1 A. Ghosh, *The Smallest Biomolecules: Diatomics and Their Interactions with Heme Proteins*, Elsevier, 2011.
2 S. W. Chung, X. Liu, A. A. Macias, R. M. Baron and M. A. Perrella, *J. Clin. Investig.*, 2008, **118**, 239–247.
3 R. Motterlini and L. E. Otterbein, *Nat. Rev. Drug Discov.*, 2010, **9**, 728–743.
4 R. Motterlini, B. Haas and R. Foresti, *Med. Gas Res.*, 2012, **2**, 1–12.
5 B. Wegiel, D. Gallo, E. Csizmadia, C. Harris, J. Belcher, G. M. Vercellotti, N. Penacho, P. Seth, V. Sukhatme, A. Ahmed, P. P. Pandolfi, L. Helczynski, A. Bjartell, J. Liao Persson and L. E. Otterbein, *Cancer Res.*, 2013, **73**, 7009–7021.
6 C. L. Hartsfield, *Antioxidants Redox Signal.*, 2002, **4**, 301–307.
7 R. Wang, *Can. J. Physiol. Pharmacol.*, 1998, **76**, 1–15.
8 A. Grilli, M. A. De Lutiis, A. Patruno, L. Speranza, F. Gizzi, A. A. Taccardi, P. Di Napoli, R. De Caterina, P. Conti and M. Felaco, *Ann. Clin. Lab. Sci.*, 2003, **33**, 208–215.
9 A. Halilovic, K. A. Patil, L. Bellner, G. Marrazzo, K. Castellano, G. Cullaro, M. W. Dunn and M. L. Schwartzman, *J. Cell. Physiol.*, 2011, **226**, 1732–1740.
10 X. Ji, K. Damera, Y. Zheng, B. Yu, L. E. Otterbein and B. Wang, *J. Pharmaceut. Sci.*, 2016, **105**, 406–416.
11 X. Ji and B. Wang, *Acc. Chem. Res.*, 2018, **51**, 1377–1385.
12 D. Wang, E. Viennois, K. Ji, K. Damera, A. Draganov, Y. Zheng, C. Dai, D. Merlin and B. Wang, *Chem. Commun.*, 2014, **50**, 15890–15893.
13 A. M. Mansour, R. M. Khaled, G. Ferraro, O. R. Shehab and A. Merlino, *Dalton Trans.*, 2024, **53**, 9612–9656.
14 A. M. Mansour, R. M. Khaled and O. R. Shehab, *Dalton Trans.*, 2024, **53**, 19022–19057.
15 A. M. Mansour, R. M. Khaled, E. Khaled, S. K. Ahmed, O. S. Ismael, A. Zeinhom, H. Magdy, S. S. Ibrahim and M. Abdelfatah, *Biochem. Pharmacol.*, 2022, **199**, 114991.
16 F. Zobi, A. Degonda, M. C. Schaub and A. Y. Bogdanova, *Inorg. Chem.*, 2010, **49**, 7313–7322.
17 E. Stamellou, D. Storz, S. Botov, E. Ntasis, J. Wedel, S. Sollazzo, B. Krämer, W. van Son, M. Seelen, H. Schmalz, A. Schmidt, M. Hafner and B. Yard, *Redox Biol.*, 2014, **2**, 739–748.
18 P. C. Kunz, H. Meyer, J. Barthel, S. Sollazzo, A. M. Schmidt and C. Janiak, *Chem. Commun.*, 2013, **49**, 4896–4898.
19 R. D. Rimmer, H. Richter and P. C. Ford, *Inorg. Chem.*, 2010, **49**, 1180–1185.
20 F. C. Wedler and R. B. Denman, *Curr. Top. Cell. Regul.*, 1984, **24**, 153–154.
21 T. Fukai and M. Ushio-Fukai, *Antioxid. Redox Signaling*, 2011, **15**, 1583–1606.
22 R. M. Khaled, M. T. Abo-Elfadl, K. Radacki, M. A. M. Abo Zeid, O. R. Shehab, N. S. Abdel-Kader, G. A. E. Mostafa, E. A. Ali, S. S. Al Neyadi and A. M. Mansour, *Dalton Trans.*, 2025, **54**, 2529–2539.
23 T. N. Moshkina, E. V. Nosova, A. E. Kopotilova, M. I. Savchuk, I. L. Nikonov, D. S. Kopchuk, P. A. Slepukhin, G. A. Kim, G. N. Lipunova and V. N. Charushin, *J. Photochem. Photobiol., A*, 2022, **429**, 113917.
24 P. S. Auti, G. George and A. T. Paul, *RSC Adv.*, 2020, **10**, 41353–41392.
25 T. Gupta, A. Rohilla, A. Pathak, M. J. Akhtar, M. R. Haider and M. S. Yar, *Synth. Commun.*, 2018, **48**, 1099–1127.
26 S. Srivastava and S. Srivastava, *Int. J. Pharma Sci. Res.*, 2015, **6**, 1206–1213.
27 D.-i. Jung, J.-h. Song, Y.-h. Kim, D.-h. Lee, Y.-g. Lee, Y.-m. Park, S.-k. Choi and J.-t. Hahn, *Bull. Kor. Chem. Soc.*, 2007, **28**, 1877.
28 S. Kasselouri, A. Garoufis, S. Paschalidou, S. P. Perlepes, I. S. Butler and N. Hadjiliadis, *Inorg. Chim. Acta*, 1994, **227**, 129–136.
29 M. A. Spackman and D. Jayatilaka, *CrystEngComm*, 2009, **11**, 19–32.
30 P. R. Spackman, M. J. Turner, J. J. McKinnon, S. K. Wolff, D. J. Grimwood, D. Jayatilaka and M. A. Spackman, *J. Appl. Crystallogr.*, 2021, **54**, 1006–1011.
31 A. M. Mansour, R. M. Khaled, K. Radacki, Z. Younes, M. Gamal, B. Guirguis, G. A. E. Mostafa, E. A. Ali and O. R. Shehab, *Dalton Trans.*, 2023, **52**, 10286–10293.
32 D. A. Habashy, R. M. Khaled, A. Y. Ahmed, K. Radacki, S. K. Ahmed, E. K. Tharwat, H. Magdy, A. Zeinhom and A. M. Mansour, *Dalton Trans.*, 2022, **51**, 14041–14048.
33 R. M. Khaled, A. Friedrich, M. A. Ragheb, N. T. Abdel-Ghani and A. M. Mansour, *Dalton Trans.*, 2020, **49**, 9294–9305.
34 A. M. Mansour, K. Radacki, R. M. Khaled, M. H. Soliman and N. T. Abdel-Ghani, *JBIC, J. Biol. Inorg. Chem.*, 2021, **26**, 135–147.
35 I. G. Dance and T. R. Miller, *J. Chem. Soc. Chem. Commun.*, 1973, 433–434.
36 P. Hemmes, J. Costanzo and F. Jordan, *J. Chem. Soc., Chem. Commun.*, 1973, 696–697.
37 D. M. Manuta and A. J. Lees, *Inorg. Chem.*, 1986, **25**, 3212–3218.
38 S. Kohlmann, S. Ernst and W. Kaim, *Angew Chem. Int. Ed. Engl.*, 1985, **24**, 684–685.
39 A. D. Becke, *Chem. Phys.*, 1993, **98**, 5648.

40 A. D. Becke, *Phys. Rev. A: At., Mol., Opt. Phys.*, 1988, **38**, 3098.
41 T. Yanai, D. P. Tew and N. C. Handy, *Chem. Phys. Lett.*, 2004, **393**, 51–57.
42 A. V. Marenich, C. J. Cramer and D. G. Truhlar, *J. Phys. Chem. B*, 2009, **113**, 6378–6396.
43 R. M. Khaled, K. Radacki, S. A. Al-Abraq, E. El-Hussieny, G. A. Mostafa, E. A. Ali, O. R. Shehab and A. M. Mansour, *Polyhedron*, 2023, **244**, 116574.
44 M. Kubeil, R. R. Vernooij, C. Kubeil, B. R. Wood, B. Graham, H. Stephan and L. Spiccia, *Inorg. Chem.*, 2017, **56**, 5941–5952.
45 R. M. Khaled, Y. S. Hegazy, M. M. Arafa, M. S. Sadek, K. Radacki, G. A. Mostafa, E. A. Ali, O. R. Shehab and A. M. Mansour, *Spectrochim. Acta, Part A*, 2024, 124644.
46 A. M. Mansour, R. M. Khaled and O. R. Shehab, *Dalton Trans.*, 2024, **53**, 19022–19057.
47 A. M. Mansour, *Eur. J. Inorg. Chem.*, 2018, **2018**, 852–860.
48 S. E. Sherman, D. Gibson, A. H.-J. Wang and S. J. Lippard, *Science*, 1985, **230**, 412–417.
49 P. M. Bruno, Y. Liu, G. Y. Park, J. Murai, C. E. Koch, T. J. Eisen, J. R. Pritchard, Y. Pommier, S. J. Lippard and M. T. Hemann, *Nat. Med.*, 2017, **23**, 461–471.
50 M. Chaves-Ferreira, I. S. Albuquerque, D. Matak-Vinkovic, A. C. Coelho, S. M. Carvalho, L. M. Saraiva, C. C. Romão and G. J. Bernardes, *Angew. Chem., Int. Ed.*, 2015, **54**, 1172–1175.
51 A. M. Mansour and O. R. Shehab, *Eur. J. Inorg. Chem.*, 2017, **2017**, 4299–4310.
52 N. Pontillo, G. Ferraro, L. Messori, G. Tamasi and A. Merlino, *Dalton Trans.*, 2017, **46**, 9621–9629.
53 D. Tripathi, N. Sakthivel, A. K. Mohanty, M. S. Kumar, U. Kumar and B. Manimaran, *Int. J. Biol. Macromol.*, 2024, 137191.
54 S. McLean, B. E. Mann and R. K. Poole, *Anal. Biochem.*, 2012, **427**, 36–40.
55 A. J. Atkin, J. M. Lynam, B. E. Moulton, P. Sawle, R. Motterlini, N. M. Boyle, M. T. Pryce and I. J. Fairlamb, *Dalton Trans.*, 2011, **40**, 5755–5761.
56 M. T. Abo-Elfadl, K. Radacki, O. R. Shehab, G. A. Mostafa, E. A. Ali and A. M. Mansour, *Bioorg. Chem.*, 2025, 108213.
57 G. M. Sheldrick, *Acta Crystallogr., Sect. A:Found. Adv.*, 2015, **71**, 3–8.
58 G. M. Sheldrick, *Acta Crystallogr., Sect. A: Found. Crystallogr.*, 2008, **64**, 112–122.
59 P. J. Hay and W. R. Wadt, *J. Chem. Phys.*, 1985, **82**, 299–310.
60 P. J. Hay and W. R. Wadt, *J. Chem. Phys.*, 1985, **82**, 270–283.
61 K. Ohno, M. Komuro, T. Sugaya, A. Nagasawa and T. Fujihara, *Dalton Trans.*, 2020, **49**, 1873–1882.
62 Y. Song, X. Lu, Y. Sheng, G. Zhao, G. Wang and Z. Geng, *J. Comput. Electron.*, 2018, **17**, 1816–1834.
63 M. J. Frisch, G. W. Trucks, H. B. Schlegel, G. E. Scuseria, M. A. Robb, J. R. Cheeseman, V. G. Zakrzewski, J. A. Montgomery, J. C. Burant, R. E. Stratmann, S. Dapprich, J. M. Millam, A. D. Daniels, K. N. Kudin, M. C. Strain, O. Farkas, J. Tomasi, V. Barone, M. Cossi, R. Cammi, B. Mennucci, C. Pomelli, C. Adamo, S. Clifford, J. Ochterski, G. A. Petersson, P. Y. Ayala, Q. Cui, K. Morokuma, D. K. Malick, A. D. Rabuck, K. Raghavachari, J. B. Foresman, J. Cioslowski, J. V. Ortiz, A. G. Baboul, B. B. Stefanov, A. L. G. Liu, I. K. P. Piskorz, R. Gomperts, R. L. Martin, D. J. Fox, T. Keith, M. A. Al-Laham, C. Y. Peng, A. Nanayakkara, C. Gonzalez, M. Challacombe, P. M. W. Gill, B. G. Johnson, W. Chen, M. W. Wong, J. L. Andres, M. Head-Gordon, E. S. Replogle and J. A. Pople, *GAUSSIAN 03 (Revision A.9)*, Gaussian Inc., Pittsburgh, 2003.
64 A. Frisch, A. B. Nielson and A. J. Holder, Gaussian, Inc., Pittsburgh, PA, 2000.
65 C. Bischof, T. Joshi, A. Dimri, L. Spiccia and U. Schatzschneider, *Inorg. Chem.*, 2013, **52**, 9297–9308.
66 A. M. Mansour, R. M. Khaled and K. Radacki, Bromo-(tricarbonyl)-[2-(pyridin-2-yl)quinoxaline]-manganese (CCDC 2453856, Experimental Crystal Structure Determination), 2025.